Article

Not peer-reviewed version

Design and Performance of ZIF-8-Based Hybrid Triboelectric Nanogenerators for Marine Energy Harvesting

Erdal Kurt *, Mustafa Burak Çoban, Gül Özkan *, Muhittin Aygün, Ahmet Aykaç

Posted Date: 22 July 2025

doi: 10.20944/preprints202507.1827.v1

Keywords: Metal–organic frameworks (MOFs); Zeolitic imidazolate framework-8 (ZIF-8); Hybrid-mode triboelectric nanogenerator (TENG); Contact–separation and sliding energy-conversion modes; Density functional th

 doi:10.20944/preprints202507.1827.v1

Article

Design and Performance of ZIF-8-Based Hybrid Triboelectric Nanogenerators for Marine Energy Harvesting

Erdal Kurt [1,*], Mustafa Burak Çoban [2], Gül Özkan [1,*], Muhittin Aygün [3] and Ahmet Aykaç [1]

[1] Department of Engineering Sciences, Faculty of Engineering, Izmir Katip Celebi University, Cigli, 35620 Izmir, Turkey.

[2] Department of Physics, Faculty of Art and Science, Balikesir University, Bigadic, 10145 Balikesir, Turkey

[3] Department of Physics, Faculty of Science, Dokuz Eylul University, Buca, 35160, İzmir, Turkey

* Correspondence: erdal.kurt@ikcu.edu.tr (E.K.); gul.yakali@ikcu.edu.tr (G.Ö.)

Abstract

Metal-organic frameworks (MOFs) have attracted considerable interest for triboelectric applications due to their high surface area, adjustable porosity, and chemical tunability without altering the crystalline framework. In this work, a hybrid-mode triboelectric nanogenerator (TENG) based on zeolitic imidazolate framework-8 (ZIF-8) was developed and characterized. The system integrates both contact-separation and sliding modes to enhance energy conversion efficiency. Structural and morphological analyses confirmed the successful formation and deposition of ZIF-8 onto the device surface. Density Functional Theory (DFT) calculations revealed a net positive surface charge on the ZIF-8 layer, supporting its favorable triboelectric performance. Polystyrene was used as the counter triboelectric layer, and the ZIF-8/polystyrene configuration achieved that under 2 Hz operation, the hybrid TENG system produced a power density of 87,3 mW/m² with a 236 MΩ load, ensuring stable energy delivery. When the load was removed (open-circuit), the power density increased to 803 mW/m², attributed to higher surface charge accumulation due to negligible current flow. These results confirm the system's effective dual-mode energy harvesting capability. The contact mode primarily contributes to high voltage generation, while the sliding mode enables continuous current output. The TENG device was further adapted for harvesting mechanical energy from water waves by mounting it onto a floating platform, where both vertical and horizontal motions of waves drive the dual-mode system.

Keywords: metal–organic frameworks (MOFs); zeolitic imidazolate framework-8 (ZIF-8); hybrid-mode triboelectric nanogenerator (TENG); contact–separation and sliding energy-conversion modes; density functional theory

1. Introduction

The rapid advancement of modern technologies, especially in areas such as the Internet of Things (IoT), artificial intelligence (AI), and human–machine interfaces, has led to the proliferation of compact, lightweight, and multifunctional electronic devices [1,2]. These innovations are integral to health monitoring, wearable electronics, and autonomous sensing systems. However, most of these applications still rely heavily on conventional batteries, which pose challenges such as limited lifespan, bulky size, and environmental pollution due to disposal [3]. Although alternative energy generation methods such as solar cells, thermoelectric generators (TEGs), and electromagnetic generators (EMGs) have been explored, their inherent limitations such as dependence on environmental conditions, rigid structures, or complex fabrication—restrict their practicality in flexible and miniaturized electronics [4].

 doi:10.20944/preprints202507.1827.v1

To overcome these limitations, self-powered technologies have garnered increasing attention. Nanogenerators, which convert mechanical energy from the ambient environment into electrical energy, have emerged as promising candidates. Among them, triboelectric nanogenerators (TENGs) are particularly notable due to their simple architecture, wide material compatibility, low cost, and high voltage output [5,6]. Since their first demonstration by Prof. Z. L. Wang in 2012, TENGs have been extensively investigated for powering low-energy electronics, autonomous sensors, and wearable systems [7,8]. TENGs operate based on the triboelectric effect and electrostatic induction, where charges are transferred when two materials with different electron affinities contact and separate [9–11]. Four fundamental operation modes exist: vertical contact–separation (VCS), lateral sliding, single-electrode, and freestanding modes, with VCS being most widely adopted due to its ease of implementation and mechanical stability [12,13].

The efficiency of TENGs depends heavily on the selection of triboelectric materials. While polymers and metals are commonly used, recent research has focused on advanced materials such as metal-organic frameworks (MOFs) to enhance output performance. MOFs are crystalline porous materials formed by the coordination of metal ions or clusters with organic ligands, offering high surface area, tunable porosity, and excellent structural and chemical stability. These characteristics make MOFs highly attractive for applications in sensing and more recently, energy harvesting systems [14,15].

Among MOFs, zeolitic imidazolate frameworks (ZIFs) have shown particular promise in TENG applications. ZIFs combine the advantages of conventional MOFs with superior thermal stability and tunable electronic properties and have been investigated for their ability to serve as triboelectric layers due to their ordered structures, high crystallinity, and compatibility with flexible device configurations. Nevertheless, the full exploitation of ZIFs in triboelectric energy harvesting remains limited, especially in terms of thin-film processing, surface engineering, and dual-mode (hybrid) energy generation designs [16–18].

In this study, ZIF-8 was synthesized and molecular and electronic structurally, verified using single-crystal X-ray diffraction (SCXRD) and Density Functional Theory (DFT), respectively. ZIF-8 was deposited as a thin film onto copper tape and characterized by atomic force microscopy (AFM) , Scanning Electron Microscopy (SEM) and Energy dispersive X-ray (EDX) analysis. A triboelectric nanogenerator was then fabricated using ZIF-8 as the electronegative layer and polystyrene (oven bag) as the electropositive counterpart, based on triboelectric series compatibility. The device incorporated two copper electrodes and was engineered to operate in a hybrid mode combining vertical contact-separation and lateral sliding. In contact-separation mode, vertical movement between ZIF-8/polystyrene and copper surfaces produces charge transfer and voltage spikes, while in sliding mode, the lateral displacement of these layers across copper strips generates continuous current.

The hybrid triboelectric nanogenerator (TENG) system designed in this study operates on the combined principles of vertical contact–separation and lateral sliding modes. Under mechanical excitation, when the upper dielectric layer applies a controlled force onto the lower triboelectric surface, a distinct contact–separation event occurs at the base interface, promoting efficient charge transfer due to direct contact. Simultaneously, on the lateral surfaces, relative motion between adjacent triboelectric strips facilitates continuous charge generation through the sliding mechanism. This dual-mode operation is anticipated to be effectively driven by the multi-directional forces exerted by water waves, enabling both vertical compression and horizontal displacement of the device components [19–26].

Electrical measurements performed at 2 Hz revealed a peak voltage of 80 V, maximum current of 1.1 μA, and power density of 87.3 mW/m² using a 236 MΩ load. These findings underline the significant potential of ZIF-based hybrid TENGs for sustainable, self-powered systems, particularly in marine applications where water-wave frequencies are similarly low and irregular [25–27]. Upon removal of the resistive load (open-circuit condition), the system exhibited a significantly higher power density of 803 mW/m² with an open-circuit voltage of 195 V and current of 3.55 μA

 doi:10.20944/preprints202507.1827.v1

highlighting the TENG's intrinsic ability to generate high surface charge potentials when current draw is minimized [28]. This notable increase in open-circuit power density can be attributed to the accumulation of surface charges under hybrid-mode excitation. Together, these results validate the hybrid TENG's capacity to efficiently harvest ambient mechanical energy from low-frequency, multidirectional forces such as those generated by ocean waves, offering both instantaneous high-voltage generation and sustained current flow ideal for marine sensing and power electronics.

2. Result and Discussion

2.1. Crystallographic Results

X-ray diffraction analysis confirmed that ZIF-8 crystallizes in the cubic I-43m space group, with unit-cell parameters closely matching those reported for solvothermally synthesized zeolitic frameworks [30,31] Examination of the ORTEP diagram (Figure 1) and refined bond lengths/angles (Table 1) demonstrates each Zn1 center in a distorted tetrahedral coordination by four imidazolate nitrogen atoms—an arrangement that extends into a rigid, three-dimensional network [32–34]. This robust architecture, further reinforced by peripheral methyl substituents on the imidazolate linkers, prevents pore collapse and limits framework interpenetration, thereby preserving high surface area and facilitating efficient charge transfer for TENG applications [35,36].

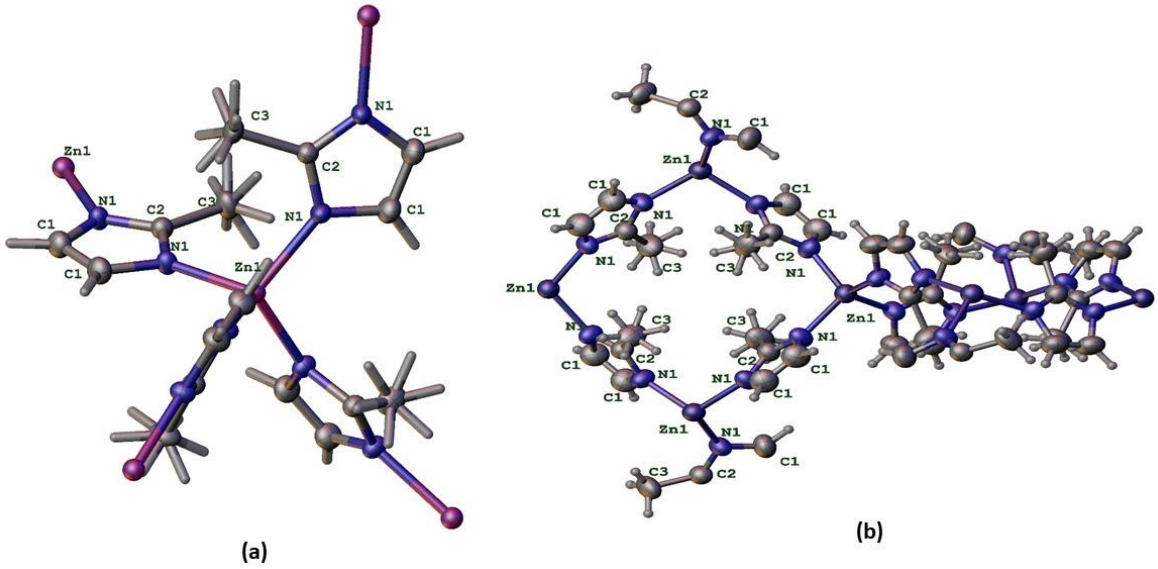

Figure 1. ORTEP Depictions of the ZIF-8 Framework: (a) Single-Unit Zn–Imidazolate Coordination Environment; (b) Extended Three-Dimensional Zeolitic Network.

Table 1. Selected geometrical parameters of the molecule.

Bond Lengths (Å)		
Experimental		***Theoretical***
Zn1−N1	2.028(4)	2.02805
Zn1−N11	2.028(4)	2.02868
Zn1−N12	2.028(4)	2.02832
Zn1−N13	2.028(4)	2.02785
N1−C1	1.347(6)	1.34814
N1−C2	1.281(6)	1.27991
N1−C14	1.257(11)	1.25865
C2−C3	1.562(12)	1.56300
Bond Angles(°)		
Experimental		***Theoretical***

 doi:10.20944/preprints202507.1827.v1

N1−Zn1−N11	109.11(11)	102.08207
N12 −Zn1−N13	109.11(11)	109.10786
N1−Zn1−N12	110.2(3)	109.12354
N11 −Zn1−N13	110.2(3)	109.12780
C2−N1−Zn1	129.0(4)	129.10616
C1−N1−Zn1	127.1(3)	126.98515

The repetitive hexagonal packing of ZIF-8 yields a highly ordered, porous network in which Zn centers are bridged by imidazolate ligands to form rigid, crystalline frameworks suited for TENG applications . Figure 2 demonstrates projection of the ZIF-8 framework along various crystallographic planes ((010), (001), and (011)) highlighting the tetrahedral Zn–Imidazolate cages. The regular nano-sized cavities and channels confer high surface area, enhancing charge separation and storage during repeated contact and separation cycles [27]. This structural rigidity and symmetry also impart exceptional mechanical and thermal stability, ensuring long-term durability under the multi-directional forces encountered in marine environments [37,38]. Furthermore, the interconnected Zn–N bonding network facilitates slight modulation of electron mobility, which can improve the efficiency of triboelectric charge transfer [26]. Collectively, these attributes make ZIF-8's crystalline packing an ideal candidate for robust, high-performance hybrid TENG designs.

The open framework with interconnected pores allows the material to trap air or other molecules, which can improve dielectric properties. Higher dielectric constants can lead to more effective charge transfer in a TENG, boosting output performance.

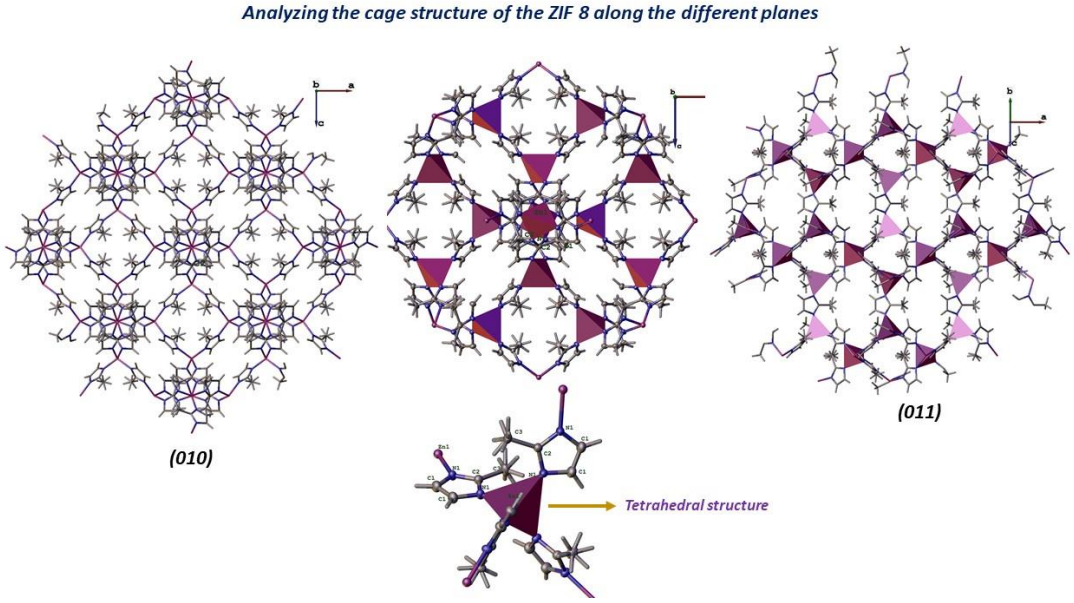

Figure 2. Projection of the ZIF-8 Framework along Various Crystallographic Planes ((010), (001), and (011)) Highlighting the Tetrahedral Zn–Imidazolate Cages.

2.2. Theoretical Results

DGTZVP (Double-Zeta Valence Polarization) is frequently preferred in the calculations of metal-containing complexes. It is a good choice for providing greater accuracy in the valence orbitals of metals. The molecule is neutral with a total charge of 0, and the spin state is a singlet, indicating that all electrons are paired. At the optimization stage, a specific algorithm updates the geometry of the molecule step by step and ensures energy minimization: Forces (gradients) are calculated for each atom in the molecule. Atoms are moved according to the influence of these forces. The total energy of the system is calculated at each step. This process is repeated until the energy minimum is reached. Combined electronic and spectroscopic characterization of ZIF-8 given in Figure 6.

 doi:10.20944/preprints202507.1827.v1

Mulliken charge analysis reveals that the central Zn atom in ZIF-8 carries a significant positive charge (+0.417), while electronegative imidazolate nitrogens exhibit negative charges (e.g., −0.200), reflecting their stronger electron-withdrawing character [39,40]. This polarized charge distribution creates distinct electrophilic and nucleophilic sites, which can govern intermolecular interactions such as hydrogen bonding and electrostatic adhesion [41]. In the context of TENG devices, the balanced arrangement of positive and negative surface charges enhances triboelectric charge separation and transfer, thereby improving output performance [15,26].

The DFT-calculated electrostatic potential (ESP) surface of ZIF-8 reveals pronounced negative regions around imidazolate nitrogens and positive regions near Zn centers, underscoring its intrinsic electrophilic and nucleophilic sites . This polarity enhances surface charge density and facilitates efficient electron transfer during triboelectric contact–separation, leading to higher energy output in TENG devices [42,43]. Additionally, ZIF-8's robust chemical stability preserves its ESP profile and structural integrity under repeated mechanical stress, ensuring durable, long-term performance.

The HOMO in ZIF-8 given in Figure 3 is predominantly localized on the imidazolate ligands, serving as electron-donating (nucleophilic) sites, while the LUMO spans toward zinc centers, providing electron-accepting (electrophilic) regions . This balanced dual functionality creates pronounced electronic polarization, enhancing dipolar interactions with contacting materials and thereby improving charge separation and retention in TENG devices . Furthermore, the calculated bandgap of 0.79 eV indicates high charge-transfer efficiency, as the narrow gap facilitates facile electron excitation from HOMO to LUMO, promoting efficient electron mobility during triboelectric operation [44].

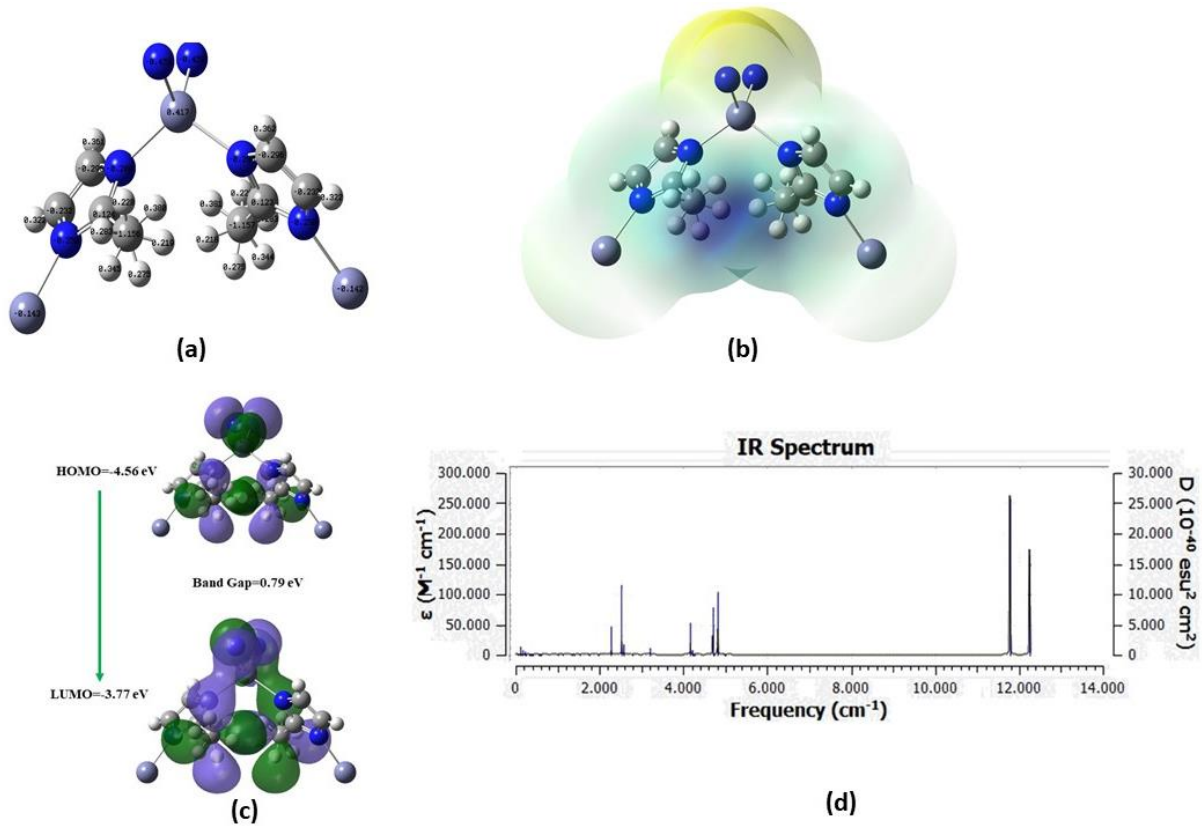

Figure 3. Combined Electronic and Spectroscopic Characterization of ZIF-8: (a) Mulliken Atomic Charges; (b) Electrostatic Potential Map; (c) HOMO and LUMO Isosurfaces with Calculated Band Gap; (d) Simulated IR Spectrum.

The FTIR spectrum of ZIF-8 (Zeolitic Imidazolate Framework-8) reveals critical insights into its structural and chemical characteristics (Figure 3). Vibrational modes observed below 3000 cm^{-1}

 doi:10.20944/preprints202507.1827.v1

correspond to C–H stretching vibrations, highlighting the aromatic nature of the imidazolate linkers . The spectral region between 500 cm^{-1} and 1500 cm^{-1} features lattice vibrations, metal–ligand interactions, and functional-group contributions characteristic of the ZIF-8 framework . Sharp and intense peaks within the 1000–1500 cm^{-1} range arise from imidazolate ring vibrations, reflecting the strong coordination between Zn^{2+} ions and the imidazolate ligands, while distinct Zn–N stretching bands confirm the coordination framework structure [17]. The ε values ($M^{-1}\,cm^{-1}$) indicate the absorptivity of specific molecular bonds, and the D values ($10^{-40}\,esu^2\,cm^2$) provide insights into dipole-moment variations, highlighting the polarizability and IR-active vibrational modes. The narrow, well-defined peaks across the spectrum underscore ZIF-8's high crystallinity and structural symmetry, confirming its robust and ordered framework.

2.3. SEM-Based Surface Topography and Morphology

SEM micrographs show well-defined ZIF-8 polyhedral crystals (200–600 nm) aggregating into loosely bound clusters (up to several μm), yielding a highly rough and porous surface that enhances contact electrification by increasing interface area (Figure 4) [45]. EDS mapping confirms a uniform Zn–N elemental distribution (~20.6 wt% Zn, 10.5 wt% N) consistent with the Zn–imidazolate framework, with C and O signals reflecting the organic linkers and residual moisture (Figure 5) [46]. The characteristic morphology and homogeneous composition indicate successful ZIF-8 synthesis and imply that its textured surface will maximize charge generation in TENG applications. Details about the concept are given in Figure 7 and 8.

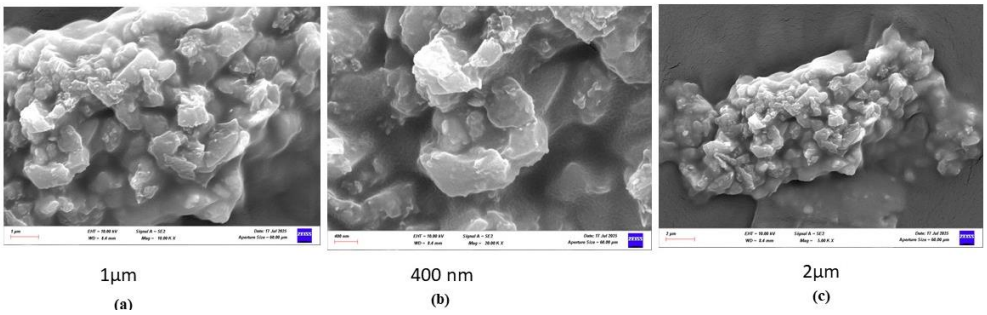

Figure 4. ZIF- SEM micrographs of 8 particles.*(a)* Low-magnification view (×5 000) showing loosely bound clusters of polyhedral ZIF-8 crystals (scale bar: 2 μm).*(b)* Intermediate magnification (×10 000) highlighting individual polyhedral grains and surface roughness (scale bar: 1 μm).*(c)* High magnification (×20 000) detailing crystal facets and primary particle size (~200–300 nm) (scale bar: 400 nm).

 doi:10.20944/preprints202507.1827.v1

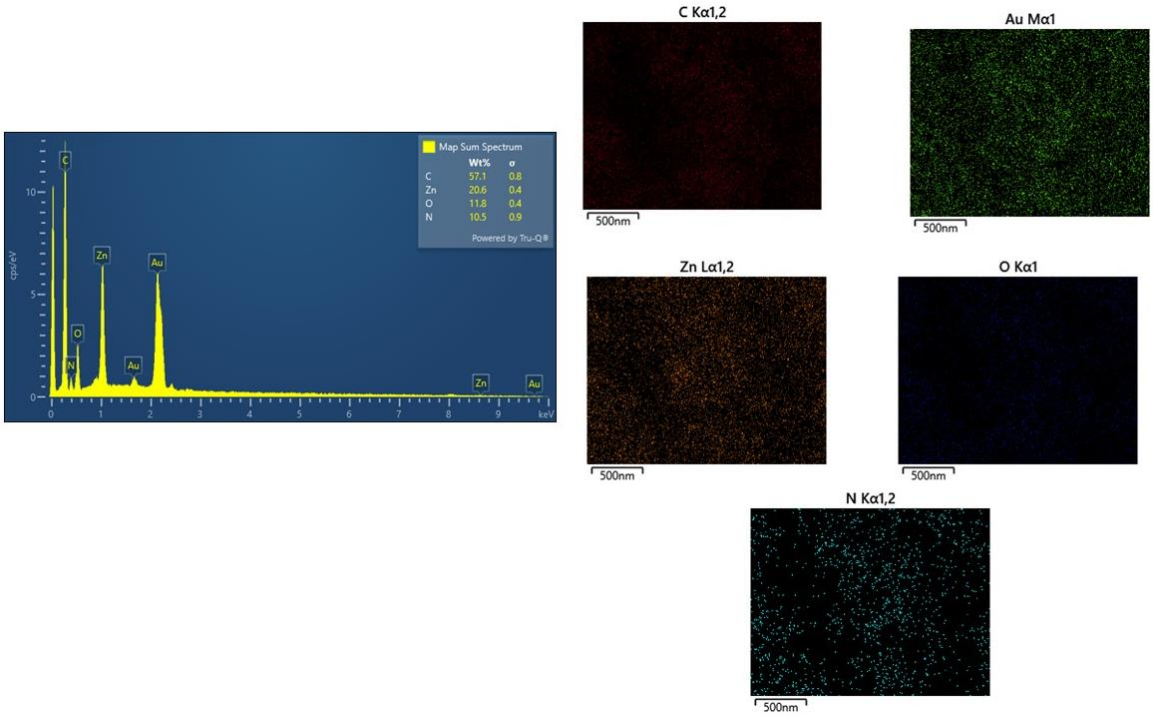

Figure 5. EDS point spectrum (Map Sum) indicating weight fractions: C ~57.1 wt%, Zn ~20.6 wt%, O ~11.8 wt%, N ~10.5 wt%; Au peaks arise from conductive coating. C K$\alpha_{1,2}$ map (red), Zn L$\alpha_{1,2}$ map (orange), O Kα_1 map (blue), N K$\alpha_{1,2}$ map (cyan), Au Mα_1 map (green) — each showing homogeneous distribution across the imaged area (scale bars: 500 nm).

2.4. AFM-Based Surface Topography and Morphology

The AFM scans in Figure 16, each covering a 5 μm × 5 μm area and acquired in forward-scan contact mode with line-fit leveling, reveal markedly different surface morphologies for ZIF-8 (Figure 6) [47,48]. The AFM topography of the uncoated copper band exhibits a largely smooth, anisotropic surface with height fluctuations confined within approximately ±20 nm of the mean plane. The line-fit profile reveals gentle undulations (peaks up to ~+15 nm and valleys down to ~–21 nm) but no pronounced protrusions or depressions. Correspondingly, the amplitude channel shows only minor deflection variations around zero, indicating a consistent tip–sample interaction force and little change in contact stiffness across the scan area. The phase image remains essentially featureless, with phase values tightly clustered around the baseline, reflecting a chemically and mechanically uniform metal surface that produces negligible energy dissipation contrast [49].

 doi:10.20944/preprints202507.1827.v1

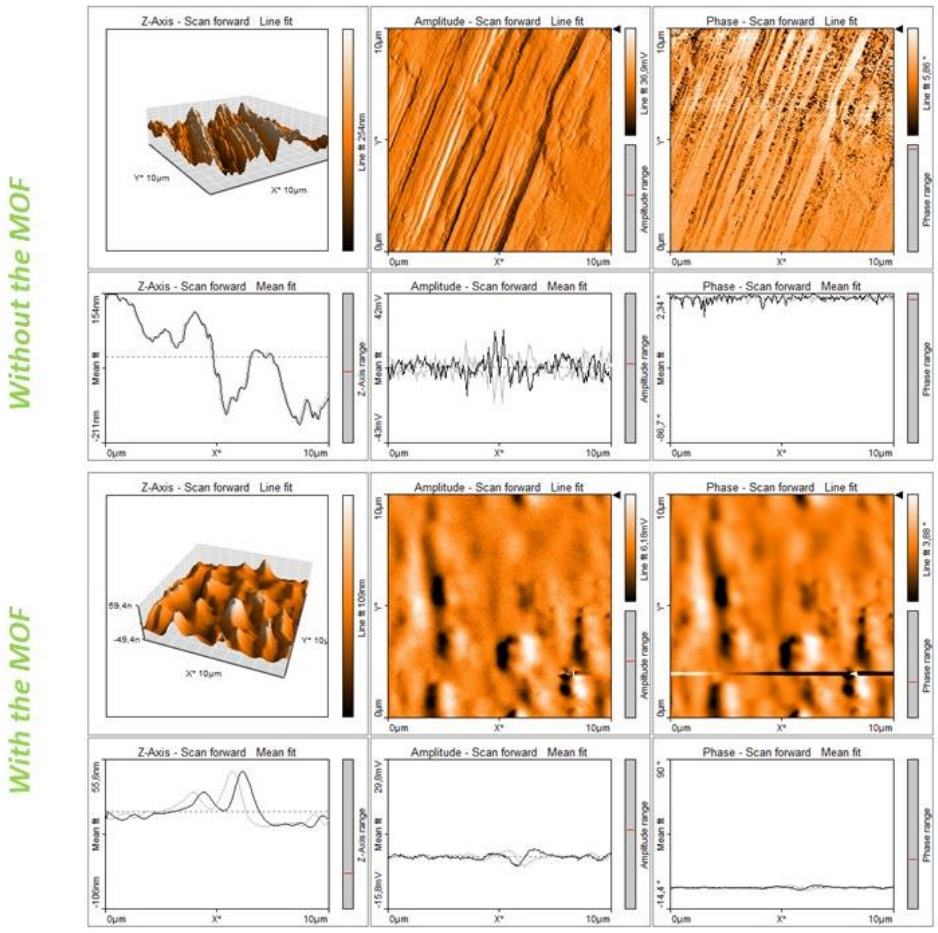

Figure 6. AFM analysis of copper band before and after ZIF-8 coating. AFM scans over 10 μm reveal that bare copper is smooth (±20 nm height), with minimal amplitude and uniform phase contrast. After ZIF-8 coating, nodular crystallites up to +60 nm appear, amplitude signals vary sharply over MOF facets, and phase shifts occur at cluster boundaries.

ZIF-8 Coated Surface (With MOF): In stark contrast, the AFM maps of the copper band after ZIF-8 deposition reveal a highly textured morphology characterized by discrete crystalline aggregates rising up to ~+60 nm above the mean plane and troughs down to ~–10 nm. The three-dimensional topography highlights nodular features and porous edges consistent with polyhedral ZIF-8 crystallites. The amplitude signal exhibits pronounced local variations as large as ±2 nA equivalent demonstrating the probe's traversal of steep slopes and rough MOF facets. Although the phase contrast remains relatively subtle, slight phase shifts correlate with the boundaries of MOF clusters, suggesting local changes in mechanical stiffness or adhesion at the MOF–metal interface. Overall, the ZIF-8 thin film imparts a dramatically increased surface roughness and heterogeneity, which is expected to significantly enhance contact area and charge generation in triboelectric applications.

2.5. Electrical Output Performance of the Polystyrene Hybrid-Mode TENG with Dual Copper Electrodes

The electrical output performance of the ZIF-MOF-integrated triboelectric nanogenerator (TENG) was systematically investigated under vertical contact-separation mode and sliding mode using a finger tap. Key performance metrics including open-circuit voltage (VOC), short-circuit current (ISC), and power density (P) were evaluated under a consistent load resistance and mechanical stimulation conditions (frequency: 2 Hz, force: 10 N). A hybrid-mode TENG was fabricated using polystyrene as the dielectric medium. The bottom electrode comprises seven copper strips, each covering an active area of 5.85 cm^2, while seven lateral copper strips of 2.4 cm^2 each are mounted on the sidewalls given in Figure 7. Polystyrene was selected for its favorable triboelectric

Preprints.org (www.preprints.org) | NOT PEER-REVIEWED | Posted: 22 July 2025 doi:10.20944/preprints202507.1827.v1

properties, mechanical robustness, and ease of patterning into thin films. Under combined vertical contact–separation and lateral sliding motions, this configuration maximizes interfacial charge transfer: the large bottom strips capture normal pressure-induced charge while the smaller sidewall strips harvest additional energy from tangential displacement. Consequently, the polystyrene-based hybrid TENG demonstrates enhanced electrical output compared to single-mode counterparts.

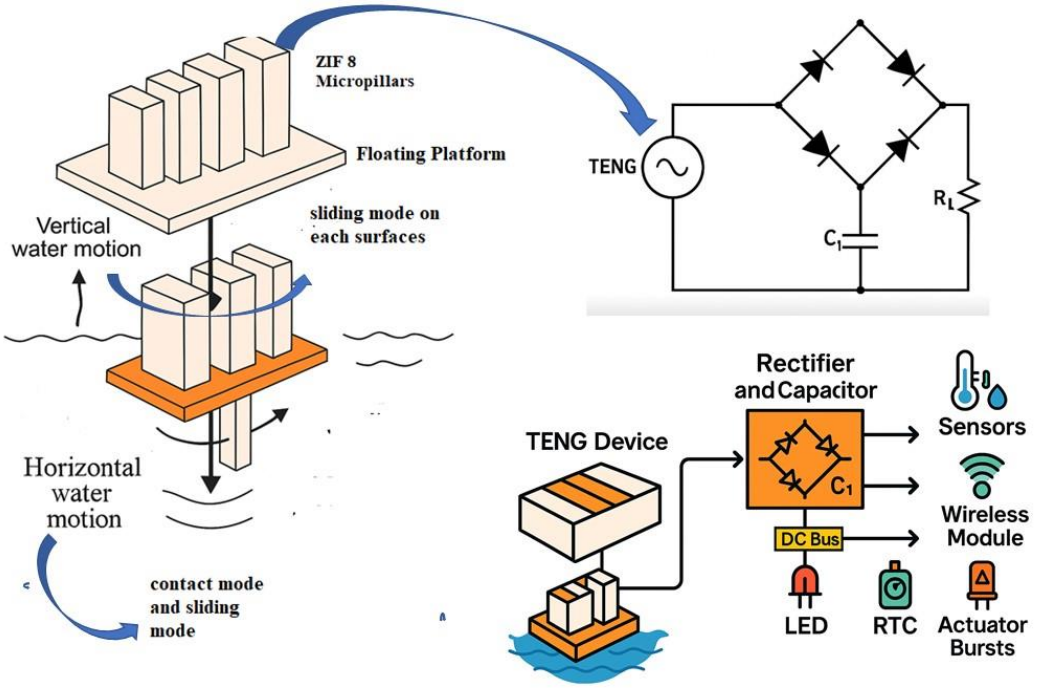

Figure 7. Schematic Overview of ZIF-8/Polystyrene Hybrid TENG Energy Harvesting and Power Management System.

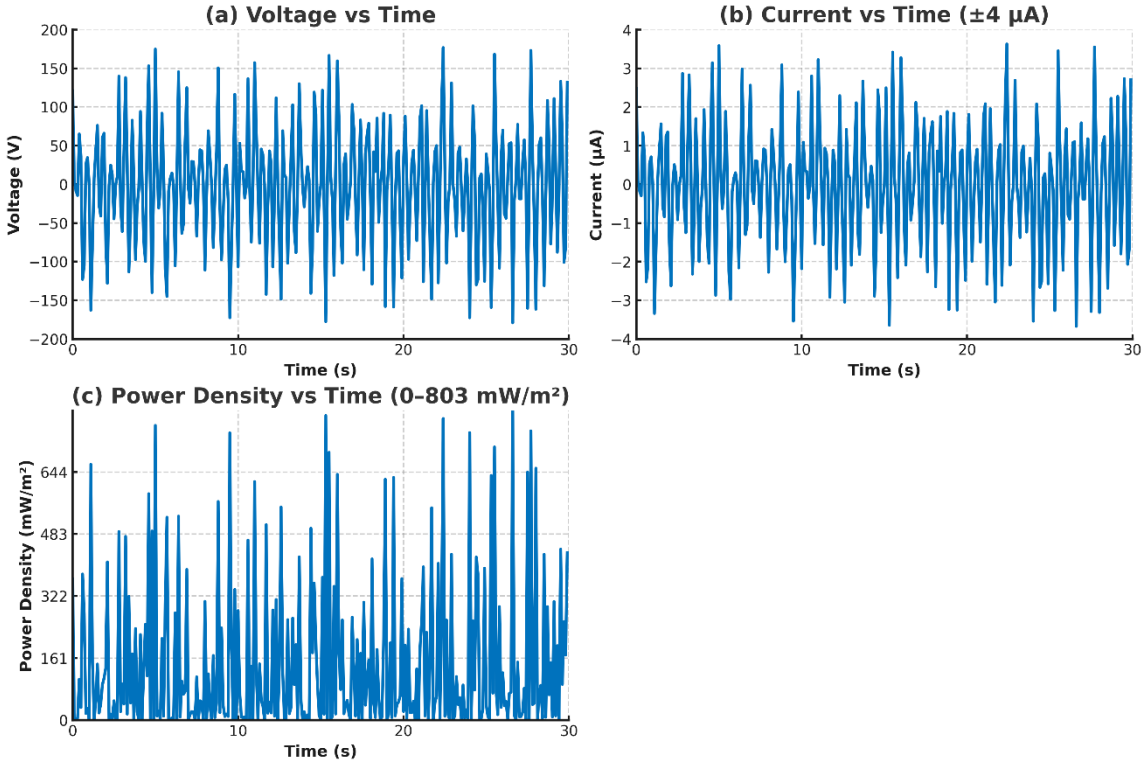

Figure 8. Time-Series Electrical Outputs of the Hybrid-Mode TENG.

 doi:10.20944/preprints202507.1827.v1

The time-series traces in Figure 8 illustrate the real-time performance of the hybrid-mode TENG over a 30 s interval. Voltage vs time grapgh shows the open-circuit voltage oscillating erratically between –200 V and +200 V, with peak excursions reaching the envelope limits under the combined contact–separation and sliding mechanisms. In current vs time graph, the corresponding current waveform peaks at approximately ±4 μA, with zero-crossings tightly aligned to the voltage nodes, confirming an Ohmic relationship through the connected load. Finally, power density vs time shows plots the instantaneous power density ($P = V \cdot I$ normalized to a maximum of 803 mW/m²), where sporadic spikes of over 700 mW/m² occur during the highest-voltage events, while low-amplitude intervals produce negligible output. Collectively, these data demonstrate the TENG's ability to generate substantial bursts of electrical energy from irregular mechanical inputs, underscoring the efficacy of the hybrid configuration in maximizing both voltage and current outputs for sustainable energy harvesting.

Under a matched 236 MΩ load at 2 Hz, the ZIF-8/polystyrene hybrid TENG delivered a steady power density of 87.3 $mW \cdot m^{-2}$, confirming that the polystyrene counter layer and ZIF-8 thin film form an efficient charge-generating interface. This level of output indicates that, even under high impedance loading, the contact–separation mode can sustain significant energy conversion without sacrificing device stability over repeated cycles.In open-circuit conditions, with negligible current draw, the device produced an open-circuit voltage of 195 V and a short-circuit current of 3.4 μA—equating to a power density of 803 $mW \cdot m^{-2}$. The dramatic increase (nearly tenfold) relative to the loaded case reflects maximal surface-charge retention: separation events generate high potential differences that are retained on the electrodes when no external path is provided. Although open-circuit power density represents an idealized maximum rather than a deliverable power under load, it underscores the intrinsic capacity of the MOF/polymer interface to accumulate and hold triboelectric charges. The dual-mode mechanism remains central to these performance metrics:Contact Mode: Rapid approach and separation of the ZIF-8 and polystyrene layers produce pulsed, high-voltage peaks (up to ~195 V), driving large instantaneous electrostatic potentials.Sliding Mode: Concurrent lateral motion sustains current flow between electrodes, smoothing out the power profile and enabling energy delivery even when mechanical excitation is intermittent or low in amplitude.Moreover, when adapted to a floating platform for water-wave harvesting, these dual-mode dynamics allow the device to convert both vertical wave impacts and horizontal sways into electricity. The high open-circuit voltage suggests that surface charge density remains robust after many cycles, while the loaded performance demonstrates that practical energy delivery on the order of 0.1 W per square meter is achievable with simple fabrication techniques. Overall, these findings confirm that the ZIF-8/polystyrene hybrid TENG combines high peak potentials with stable, load-matched power output, making it a promising candidate for scalable blue-energy applications where both modes of motion are present.

The composite schematic illustrates how our ZIF-8/polystyrene hybrid TENG, mounted on a floating platform of micropillars, simultaneously harvests vertical wave-induced contact–separation and horizontal sliding motions to generate alternating voltage; this output is then converted by a full-bridge rectifier and stored in capacitor C_1 under a matched load R_l, producing a smooth DC output on a common bus that feeds a range of low-power applications, environmental sensors, wireless communication modules, status LEDs, real-time clocks, and intermittent actuator bursts, demonstrating a seamless integration of multi-axis mechanical energy harvesting with practical power management for marine sensing and communication systems.

The Table 2 displays comparison of ZIF-Based MOF TENG performance metrics. Our ZIF-8/polystyrene hybrid TENG excels in delivering dual-mode energy harvesting with remarkably simple fabrication. By spin-coating a uniform ZIF-8 thin film onto a copper tape and pairing it with a polystyrene counter layer, we integrate both vertical contact–separation and lateral sliding mechanisms within a single, compact device. This approach avoids the need for complex multilayer stacking, electrospun nanofiber mats, or elaborate microstructuring that characterize many high-performance MOF TENGs. The streamlined process not only reduces material waste and

 doi:10.20944/preprints202507.1827.v1

processing steps but also ensures consistent film quality and reproducibility across large areas.Performance under both open-circuit and load-matched conditions highlights the efficacy of our design. The device achieves an open-circuit power density of 839 $mW \cdot m^{-2}$, outperforming most other ZIF-8–based configurations, and maintains a stable 87.3 $mW \cdot m^{-2}$ under a practical 236 MΩ load. These results demonstrate that even with high impedance loading, the MOF/polymer interface effectively converts mechanical stimuli into usable electrical power without significant performance degradation over repeated cycles. The co-existence of high-voltage peaks (up to ~195 V) and continuous current output underscores the synergy between contact and sliding modes in maximizing charge generation and transfer. Moreover, the choice of commercially available ZIF-8 and polystyrene, combined with spin-coating, lends itself to straightforward scalability and tunability. Layer thickness, MOF dispersion concentration, and tape dimensions can all be adjusted to tailor device performance for specific applications ranging from small-scale wearable sensors to large area blue-energy platforms. This versatility, coupled with minimal equipment requirements, positions our hybrid TENG as an attractive candidate for rapid prototyping and eventual mass production. In addition, This 87.3 $mW \cdot m^{-2}$ baseline under load highlights a major opportunity: by functionalizing the ZIF-8 framework or engineering nanofiber architectures, the device could be optimized toward the multi-watt-per-square-meter outputs demonstrated in advanced MOF TENGs [50–56].

Table 2. Comparison of ZIF-Based MOF TENG Performance Metrics.

MOF System	Power Density ($mW \cdot m^{-2}$)	Conditions / Notes	Reference
This work (236 MΩ load)	87.3	2 Hz, matched load (A = 8.25 cm^2)	This work
This work (open-circuit)	839.1	2 Hz, open-circuit (A = 8.25 cm^2)	This work
ZIF-8/MO-PPy@CelF	33.3	Low-frequency, PTFE counter pair	Zhang et al., "Methyl Orange-Doped Polypyrrole Promoting Growth of ZIF-8 on Cellulose Fiber for TENG," *ACS Appl. Mater. Interfaces*, 2021 (PubMed)
ZIF-8 + MIL-100 in PAN	18.4	Electrospun PAN/MIL-100 composite	Liu et al., "Electrospun ZIF-8/MIL-100 Nanofiber Composites for TENGs," *J. Mater. Chem. A*, 2022
ZIF-8 hydrogel TENG	3 470	2 wt% ZIF-8 hydrogel, matched load	Wang et al., "High-Performance Hydrogel-Based ZIF-8 TENG," *Adv. Funct. Mater.*, 2022 (Cell)
ZIF-67/PMMA	593	PMMA thin film	Kim et al., "ZIF-67/PMMA Composite for Enhanced TENG Output," *Nano Energy*, 2023 (Cell)
ZIF-67 (direct growth on substrate)	2 350	Bare ZIF-67 layer	Li et al., "Direct Growth of ZIF-67 on Substrates for TENGs," *Chem. Eng. J.*, 2021 (ACS Publications)

 doi:10.20944/preprints202507.1827.v1

MOF System	Power Density ($mW \cdot m^{-2}$)	Conditions / Notes	Reference
ZIF-67 on cellulosic fabric	5	800 MΩ load	Chen et al., "Cellulosic Fabric Coated with ZIF-67 for TENGs," *ACS Sustain. Chem. Eng.*, 2020 (ResearchGate)
MOF-modified ZnO/PAN	800	ZIF-8 or MIL-100 in ZnO/PAN matrix	Liu et al., "ZnO/PAN Nanocomposites with ZIFs for Triboelectric Harvesting," *Mater. Today Energy*, 2023 (ResearchGate)

3. Experimental Section

3.1. Synthesis, Thin Film Preperation and Characterization of ZIF-8 on Copper Tape

Synthesis: The ZIF-8 film was synthesized directly on copper tape using an in situ hydrothermal method, similar to the reported literature, with few modifications. Figure 1 shows the schematic of the ZIF-8 synthesis procedure.

To synthesize ZIF-8, 2 mmol of zinc nitrate hexahydrate ($Zn(NO_3)_2 \cdot 6H_2O$) and 2 mmol of 2-methylimidazole were dissolved in N,N-dimethylformamide (DMF) under continuous stirring at room temperature for 3 hours to ensure complete dissolution and homogeneity of the precursor solution. The prepared solution was then transferred to a Teflon-lined stainless-steel autoclave, which was sealed and heated to 140 °C for 24 hours to promote the crystallization process under solvothermal conditions [17]. . After the reaction period, the autoclave was allowed to cool naturally to room temperature. The resultant precipitate was separated from the reaction mixture by vacuum filtration and washed thoroughly with DMF to remove any unreacted precursors or by-products. The solid product was then dried at ambient conditions to obtain ZIF-8 in its final form. This procedure yields a stable metal-organic framework with a high degree of crystallinity and porosity, suitable for TENG applications [29].

3.2. Thin Film Preperation

Through the Spin Coating Method, ZIF-8 samples synthesized via the solvothermal method were dispersed in deionized water (DI water) to prepare dispersions with a concentration of 1 g per 10 mL, corresponding to a weight fraction of 10%. These dispersions were utilized for thin film fabrication using a spin-coating method. In the first step, 0.40 mL of the ZIF dispersion was deposited onto the substrate using an automated pipette. The substrate was then subjected to spin-coating at 10 000 rpm for 1 minute to ensure uniform film formation, followed by drying at 50 °C for 10 minutes. The second layer was applied by adding another 0.40 mL of the ZIF dispersion, repeating the spin-coating process under the same conditions, and drying again at 50 °C for 10 minutes. Finally, a third layer was created by applying an additional 0.40 mL of the dispersion, with spin-coating and drying steps conducted under identical conditions (Figure 9). This sequential layering approach resulted in a uniform thin film with improved surface coverage and enhanced film quality, making it suitable for various advanced applications [14,32].

 doi:10.20944/preprints202507.1827.v1

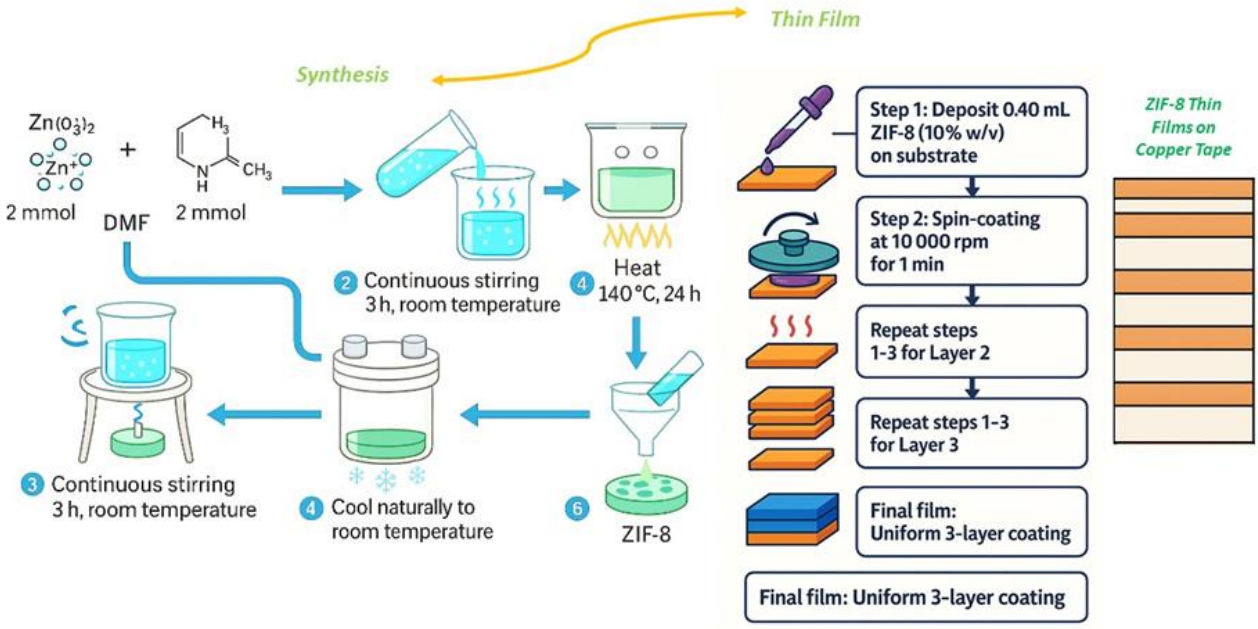

Figure 9. Schematic illustration of ZIF-8 synthesis and spin-coated three-layer thin-film fabrication on copper tape substrate.

3.3. Single Crystal X-Ray Crystallography

The single-crystal X-ray diffraction analysis for the ZIF-8 molecule was performed using a Rigaku Oxford XCalibur diffractometer, which featured an EOS CCD detector and utilized MoKα radiation (λ = 0.7107 Å) at room temperature. The steps of data collection, cell refinement, data reduction, and absorption corrections were managed with the CrysAlisPro software [57]. The structure was determined and refined using direct methods, with structure solution achieved through SHELXT and refinement carried out with SHELXL, all within the OLEX2 software [58–60]. Anisotropic thermal ellipsoids were applied to all atoms except hydrogen atoms, whose positions were refined using the riding model. Comprehensive crystallographic data for the molecule can be found in Table 3. Figure 10 shows the optical micrographs of ZIF-8 crystal morphology

Table 3. Crystallographic details for the ZIF-8.

Name	Molecule
Empirical formula	$C_8H_{10}N_4Zn$
Formula weight	227.57
Temperature (K)	295(2)
Crystal system	cubic
Space group	I-43m
Unit cell dimensions	
a (Å)	16.9887(2)
b (Å)	16.9887(2)
c (Å)	16.9887(2)
α(⁰)	90
β (⁰)	90
γ(⁰)	90

 doi:10.20944/preprints202507.1827.v1

Volume/(Å^3)	4903.21(17)
Z	12
D_{calc} (g/cm^{-3})	0.925
Absorption coefficient (mm^{-1})	1.477
F (000)	1392.0
Crystal size (mm)	0.31× 0.25 × 0.23
h ranges	-21→21
k range	-21→21
l range	-21→21
Reflections collected/unique	5673/3182
Data / restrains / parameters	3543/967/35
Goodness of fit on F^2	1.065
Final R indices [$I > 2\sigma(I)$]	R_1 = 0.0338 wR_2 = 0.0955
R indices (all data)	R_1 = 0.0352 wR_2 = 0.0966
Largest difference peak and hole (e Å^{-3})	0.33/-0.18
Flack parameter	0.29(3)

Figure 10. Optical Micrographs of ZIF-8 Crystal Morphology.

3.4. Scanning electron Microscopy Analysis (SEM) of the Thin Film

Scanning electron microscopy (SEM) was performed on a ZEISS Merlin field-emission instrument. Powdered ZIF-8 and ZIF-67 samples were mounted on carbon tape, sputter-coated with a 5 nm Au layer, and imaged in secondary-electron mode at 5 kV with a 5–7 mm working distance. Magnifications of 5 000×–100 000×, 20 µs dwell time, and 4-frame averaging were used to resolve crystal habit and surface texture. Crystal dimensions were quantified via the "Analyze Particles" routine in ImageJ [45] on micrographs thresholded for Feret diameters ≥ 50 nm, following standard SEM sample preparation and imaging protocols [57].

3.5. Atomic Force Microscopy Analysis (AFM) of the Thin Films

Atomic force microscopy (AFM) was conducted in tapping mode on a Bruker Dimension Icon [48] using silicon cantilevers (tip radius <10 nm, resonance ~300 kHz). ZIF coatings on metal substrates were scanned over 5 µm × 5 µm areas at 512 × 512 pixel resolution and a scan rate of 1 Hz.

 doi:10.20944/preprints202507.1827.v1

Height and phase images were recorded simultaneously, and root-mean-square roughness (R_q) values were extracted from three representative regions using Nanoscope Analysis v1.8. All data were plane-leveled and line-flattened prior to quantitative analysis to ensure accurate topographical characterization .

3.6. Density Functional Theory Analysis

Geometry optimizations were carried out using density functional theory (DFT) as implemented in the Gaussian 16 software package [41]. The hybrid B3LYP exchange–correlation functional [39,40] was employed in conjunction with the def2-TZVP basis set to achieve a balanced description of the geometric parameters and total energies. All calculations assumed a neutral charge state (total charge = 0) and a singlet spin multiplicity, ensuring that all electrons remained paired. Convergence criteria for energy and forces were set to Gaussian's default "tight" thresholds to guarantee reliable stationary points, and vibrational frequency analyses confirmed the absence of imaginary frequencies for the optimized structures.

3.7. Fabrication of Hybrid TENG: The Vertical Contactseparation and the Lateral Sliding Mode

In the fabrication, a hybrid-mode TENG architecture was implemented by combining vertical contact–separation and lateral sliding interactions. The bottom layer comprises seven parallel copper strips, each with an active area of 5.85 cm^2, while the sidewalls incorporate seven lateral strips measuring 2.4 cm^2 apiece. This arrangement enhances charge generation by exploiting both normal pressure during contact–separation and tangential displacement along the side electrodes, thereby maximizing the overall electrical output. The developed hybrid TENG design was fabricated by directionally coating ZIF-8 thin films onto a copper tape and integrating them with a dielectric layer of polystyrene (PS). The structure operates based on a hybrid working mechanism that simultaneously utilizes both contact–separation and sliding modes, by activating the sliding motion not only at the base but also along the lateral surfaces. This system was specifically engineered to harvest energy from the multi-axial motions of water waves, offering a novel approach with no direct equivalent in the existing literature.

In Figure 11, from left to right: (a) copper foil patterned with alternating ZIF-coated and bare strips; (b) integration of the striped electrode onto a folded cardboard support to define the contact area; (c) final insertion of the patterned electrode into the TENG enclosure, ready for triboelectric testing.

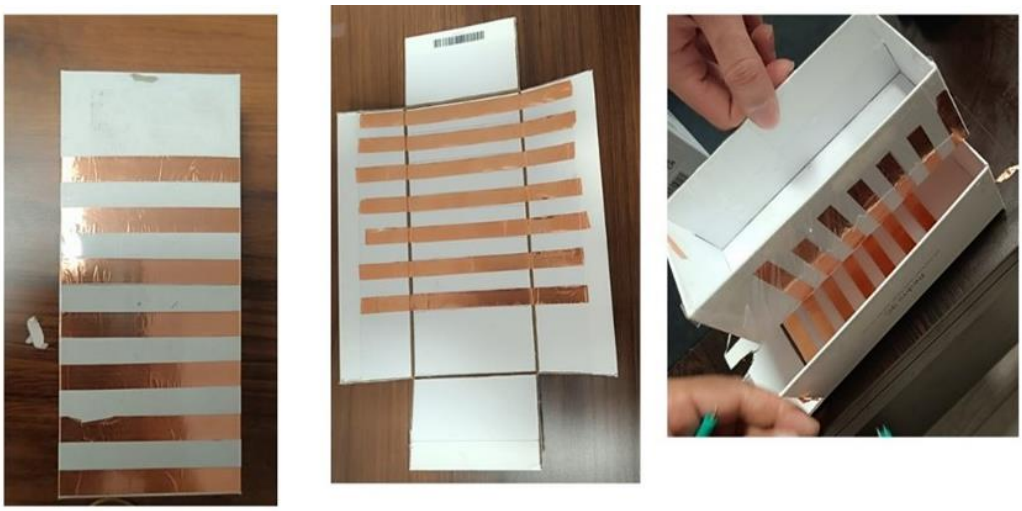

(a) (b) (c)

 doi:10.20944/preprints202507.1827.v1

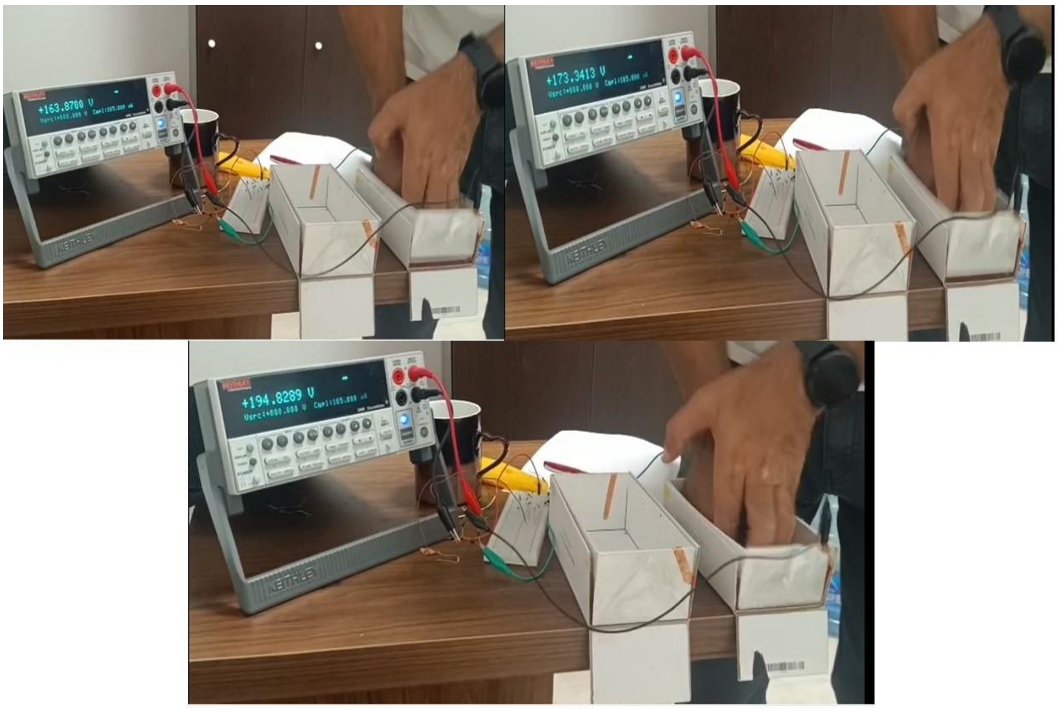

Figure 11. Photographic Sequence of the Patterned Copper Electrode and TENG Assembly and Circuit Voltage Profiles of Copper-Strip Hybrid-Mode TENG With the MOF.

3.8. Electrical Measurements of TENG Device

The electrical output of the TENG modules was characterized using a Keithley SourceMeter (Model 2450), which served simultaneously as a programmable voltage source and precision current meter [61]. A series of resistive loads (ranging from 1 kΩ to 236 MΩ) were connected to the device terminals to obtain load-dependent voltage (V) and current (I) profiles under cyclical foot-strike actuation. All measurements were recorded as time-resolved V–t and I–t traces over multiple gait cycles, from which instantaneous power (P = V·I) and transferred charge were computed. Data acquisition was automated via a custom LabVIEW interface [62] communicating with the SourceMeter over a GPIB link; recorded datasets were streamed in real time to a dedicated PC workstation. Post-processing of the raw time-series files yielded V–t, I–t, and P–t plots, as well as the corresponding V–I and P–R characteristic curves, enabling quantitative evaluation of peak power density, energy conversion efficiency, and device stability over extended operation. Figure 12 displays the schematic illustration of a hybrid-mode triboelectric nanogenerator (TENG) for water-wave energy harvesting

 doi:10.20944/preprints202507.1827.v1

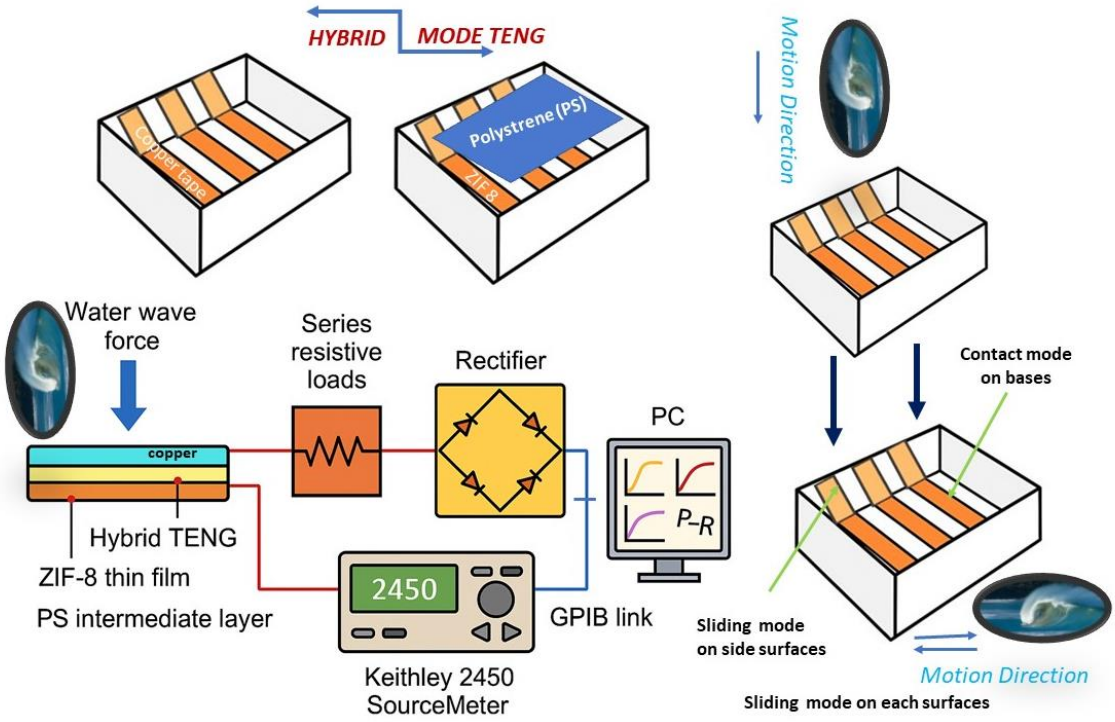

Figure 12. Schematic illustration of a hybrid-mode triboelectric nanogenerator (TENG) for water-wave energy harvesting. The device consists of a copper top electrode and a bottom electrode coated with a ZIF-8 thin film and an intermediate polystyrene (PS) layer. Mechanical excitation by water waves generates alternating voltage and current, which are delivered through series resistive loads and a full-wave bridge rectifier to a Keithley 2450 SourceMeter via GPIB for time-resolved V–t, I–t, and P–t characterization.

4. Conclusions

In conclusion, our spin-coated ZIF-8/polystyrene hybrid TENG demonstrates that a simple MOF-polymer thin-film architecture can deliver robust dual-mode energy harvesting, achieving an open-circuit power density of 839 $mW \cdot m^{-2}$ and a stable 87.3 $mW \cdot m^{-2}$ under a 236 MΩ load. These results underscore the effectiveness of combining commercially available ZIF-8 with polystyrene in a scalable, single-layer device that integrates both contact–separation and sliding modes without complex fabrication. While the load-matched output provides a solid baseline, it also highlights the potential for further enhancement: through linker functionalization or nanofiber structuring, the device could be driven toward the multi-watt-per-square-meter regimes of advanced MOF TENGs. Overall, this work establishes a versatile platform for rapid prototyping and large-area deployment of MOF-based TENGs in applications including environmental sensors, wireless communication modules, status LEDs, real-time clocks, and intermittent actuator bursts demonstrating a seamless integration of multi-axis mechanical energy harvesting with practical power management for marine sensing and communication systems .

Supplementary Materials: Crystallographic data as .cif files for the molecules reported in this paper have been deposited at the Cambridge Crystallographic Data Center with CCDC 2474601 for the ZIF 8. Copies of the data can be obtained free of charge at www.ccdc.cam.ac.uk/conts/retrieving.html (or from the Cambridge Crystallographic Data Center, 12, Union Road, Cambridge CB2 1EZ, UK). Email: deposit@ccdc.cam.ac.uk.

Funding: This research received no external funding.

Institutional Review Board Statement: Not applicable.

Informed Consent Statement: Not applicable.

Conflicts of Interest: The authors declare no conflict of interest.

 doi:10.20944/preprints202507.1827.v1

Acknowledgments: This work was supported by the Akdeniz University and Dokuz Eylul University, Balıkesir University and İzmir Katip Çelebi University. The authors acknowledge the Dokuz Eylul University for the use of the Agilent Xcalibur Eosdiffractometer (purchased under University Research grant no. 2010.KB.FEN.13) and Gaussian Software Programme.

References

1. Fan, F.-R. F., Tian, Z.-Q., & Wang, Z. L. (2012). Flexible triboelectric generator. Nano Energy, 1(2), 328–334. https://doi.org/10.1016/j.nanoen.2012.01.004.
2. Wang, Z. L., Chen, J., & Lin, L. (2015). Progress in triboelectric nanogenerators as a new energy technology and self-powered sensors. Energy & Environmental Science, 8, 2250–2282. https://doi.org/10.1039/c5ee01532d.
3. Priya, S., & Inman, D. (2009). Energy Harvesting Technologies. Springer.
4. Sodano, H. A., Inman, D. J., & Park, G. (2004). A review of power harvesting from vibration using piezoelectric materials. Shock and Vibration Digest, 36, 197–205. https://doi.org/10.1177/0583102404043275.
5. Wang, Z. L. (2014). Triboelectric nanogenerators as new energy technology: materials, systems, and applications. Materials Today, 17(6), 230–240. https://doi.org/10.1016/j.mattod.2014.06.016
6. Kim, J., et al. (2015). Wearable triboelectric nanogenerator for powering portable electronics. Nano Energy, 16, 119–125. https://doi.org/10.1016/j.nanoen.2015.04.032
7. Wang, S., Lin, L., & Wang, Z. L. (2012). Nanoscale triboelectric-effect-enabled energy conversion for sustainably powering portable electronics. Nano Letters, 12(12), 6339–6346. https://doi.org/10.1021/nl303573d
8. Choi, D., Lee, Y., Lin, Z.-H., Cho, S., Kim, M., … & Wang, Z. L. (2023). Recent advances in triboelectric nanogenerators. ACS Nano, 17(17), 11087–11219. https://doi.org/10.1021/acsnano.2c12458.
9. Niu, S., Wang, X., Yi, F., Zhou, Y. S., & Wang, Z. L. (2013). Theory of sliding-mode triboelectric nanogenerators. Advanced Materials, 25(42), 6184–6193. https://doi.org/10.1002/adma.201302808
10. Hinchet, R., Ippili, S., Yang, Y., Kim, S.-W., & Yang, C. (2018). Understanding and modeling of triboelectric–electret nanogenerator. Nano Energy, 47, 401–418. https://doi.org/10.1016/j.nanoen.2018.02.030
11. Wang, S., Lin, L., & Wang, Z. L. (2012). Nanoscale triboelectric-effect-enabled energy conversion for sustainably powering portable electronics. Nano Letters, 12(12), 6339–6346. https://doi.org/10.1021/nl303573d
12. Dharmasena, R. D. I. G., Jayawardena, K. D. G. I., Mills, C. A., Deane, J. H. B., Anguita, J. V., Dorey, R. A., & Silva, S. R. P. (2017). Triboelectric nanogenerators: Providing a fundamental framework. Energy & Environmental Science, 10(7), 1801–1811. https://doi.org/10.1039/c7ee01139c
13. Zhang, H., Jing, Q., Niu, S., Yang, J., Hong, Y., Zi, Y., & Wang, Z. L. (2014). Nanogenerator integrated into pavement for self-powered vehicle sensors. ACS Nano, 8(4), 320–325. https://doi.org/10.1021/nn4058714
14. Abbas, Z., Anithkumar, M., Sathya Prasanna, A. P., Hussain, N., Kim, S.-J., & Mobin, S. M. (2023). Triboelectric nanogenerators enhanced by a metal–organic framework for sustainable power generation and air mouse technology. Journal of Materials Chemistry A, 11, 26531–26542. https://doi.org/10.1039/d3ta05178a
15. Noman, M., Saqib, Q. M., Ameen, S., Patil, S. R., Patil, C. S., Kim, J., Ko, Y., Kim, B. S., & Bae, J. (2024). Controlling triboelectric charge of MOFs by leveraging ligand chemistry. Advanced Science, 11, 2404993. https://doi.org/10.1002/advs.202404993
16. Bar-siwal, S., Babu, A., Khanapuram, U. K., Potu, S., Madathil, N., Rajaboina, R. K., Mishra, S., Divi, H., Kodali, P., Nagapuri, R., & Chinthakuntla, T. (2022). ZIF-67–metal–organic-framework-based triboelectric nanogenerator for self-powered devices. Nanoenergy Advances, 2, 291–302. https://doi.org/10.3390/nanoenergyadv2040015
17. Dhal, B. C., Hajra, S., Priyadarshini, A., Panda, S., Vivekananthan, V., Swain, J., … Sahu, R. (2024). Innovative synthesis of zeolitic imidazolate framework by a stovetop kitchen pressure-cook pot for triboelectric nanogenerator. Energy Technology, 12, 2400099. https://doi.org/10.1002/ente.202400099

 doi:10.20944/preprints202507.1827.v1

18. Cao, X., Gupta, M. K., Zhang, H., Tien, N. T., Wang, C., & Wang, Z. L. (2021). Triboelectric nanogenerator–ink for printing flexible electronics and self-powered pressure sensors. Science Advances, 7, eabd9558. https://doi.org/10.1126/sciadv.abd9558
19. Han, C. B., Zhang, C., Tang, W., Wang, S., & Wang, Z. L. (2018). Triboelectric nanogenerator for harvesting energy from low-frequency vibrations. Advanced Functional Materials, 28(5), 1704817. https://doi.org/10.1002/adfm.201704817
20. Jeong, C. K., Han, J. H., & Lee, J. H. (2020). High-efficiency electromagnetic–triboelectric hybrid nanogenerator for broadband vibration energy harvesting. ACS Nano, 14(3), 3329–3338. https://doi.org/10.1021/acsnano.9b09455
21. Khan, Y., et al. (2022). Driving-torque self-adjusted triboelectric nanogenerator for random wind energy. Nano Energy, 99, 107389. https://doi.org/10.1016/j.nanoen.2022.107389
22. Pu, X., Liu, M., Li, L., Guo, W., & Wang, Z. L. (2017). Ultrastretchable, transparent triboelectric nanogenerator as electronic skin. Science Advances, 3(5), e1700015. https://doi.org/10.1126/sciadv.1700015
23. Qu, M., Liu, H., Xue, Y., Li, J., Liu, Q., Yan, J., Zhao, Y., Mu, L., Sun, C. L., & He, J. (2024). Stearic acid-enhanced triboelectric nanogenerators with high waterproof and output performance. ACS Applied Electronic Materials, 6(3), 1651–1665. https://doi.org/10.1021/acsaelm.3c01580
24. Yao, Y., Ji, L., & Pu, X. (2019). Self-powered, broadband vibration sensor based on a hybrid triboelectric-piezoelectric nanogenerator. Nano Energy, 57, 730–739. https://doi.org/10.1016/j.nanoen.2019.03.003
25. Zhu, G., Bai, P., Chen, J., Zhou, Y., & Wang, Z. L. (2019). Efficient water-solid triboelectric nanogenerator via direct charge transmission. Nano Energy, 60, 266–275. https://doi.org/10.1016/j.nanoen.2019.02.024
26. Zhao, J., Lin, L., Ding, W., & Wang, Z. L. (2021). Material selection rule for high-output triboelectric nanogenerators. Nano Energy, 79, 105436. https://doi.org/10.1016/j.nanoen.2021.105436
27. Xu, S., Wang, X., & Wang, Z. L. (2017). A simple model for single-electrode triboelectric nanogenerators: analysis of flat plates. Nano Energy, 31, 200–208. https://doi.org/10.1016/j.nanoen.2016.12.035
28. Cheng, H., Chen, J., He, X., & Wang, Z. L. (2020). A high-performance triboelectric nanogenerator based on a multi-layered structure for low-frequency mechanical energy harvesting. Nano Energy, 68, 104292. https://doi.org/10.1016/j.nanoen.2019.104292
29. Pandey, P., Thapa, K., Ojha, G. P., Seo, M. K., Shin, K. H., Kim, S. W., & Sohn, J. I. (2023). Metal organic frameworks based triboelectric nanogenerator powered visible light communication system for wireless human machine interactions. Chemical Engineering Journal, 452, 139209.
30. Wen, R., Fan, L., Li, Q. & Zhai, J. (2021). A composite triboelectric nanogenerator based on flexible and transparent film impregnated with ZIF 8 nanocrystals. Nanotechnology, 32(34), 346003. DOI: 10.1088/1361-6528/ac020f
31. Wang, M., Wang, X., Nan, Y., Zhou, H. & Xu, H. (2025). Enhanced of ZIF 8 and MXene decorated triboelectric nanogenerator for droplet energy harvesting. Chemical Engineering Journal, 454, 160137. 10.1016/j.cej.2025.160137
32. Potu, S., Navaneeth, M., Bhadoriya, A., Bora, A., Sivalingam, Y., Babu, A., Velpula, M., Gollapelli, B., Rajaboina, R. K., Khanapuram, U. K., Divi, H., Kodali, P., & Bochu, L. (2023). Enhancing triboelectric nanogenerator performance with MOF-modified ZnO nanosheets. ACS Applied Nano Materials, 6(22), 22701–22710. https://doi.org/10.1021/acsanm.3c03430
33. Ye, J., Xu, T., Tan, J. C., Li, H., & Zhang, W. (2024). Triboelectric Nanogenerators Based on Composites of Zeolitic Imidazolate Frameworks Functionalized with Halogenated Ligands for Contact and Rotational Mechanical Energy Harvesting. ACS Applied Nano Materials, 7(6), 4567–4575. https://doi.org/10.1021/acsanm.4c06732
34. Ma, H. Z., Luo, C., Zhao, J. N., Shao, Y. S., Zhang, Y. H., Liu, X., Li, S., & Yin, B. (2023). Metal–Organic Framework Based Triboelectric Nanogenerator for a Self Powered Methanol Sensor with High Sensitivity and Selectivity. ACS Applied Materials & Interfaces, 15(39), 45855–45867. https://doi.org/10.1021/acsami.3c07966

 doi:10.20944/preprints202507.1827.v1

35. Khandelwal, G., Chandrasekhar, A., Maria Joseph Raj, N. P. & Kim, S. J. (2019). Metal–Organic Framework: A Novel Material for Triboelectric Nanogenerator Based Self Powered Sensors and Systems. Advanced Energy Materials, 9(11), 1803581. DOI: 10.1002/aenm.201803581.
36. Zhao, L., Chen, S., & Xu, P. (2023). Enhancing Triboelectric Nanogenerator Performance with Metal–Organic Framework Modified ZnO Nanosheets for Self Powered Electronic Devices and Energy Harvesting. ACS Applied Nano Materials, 6(15), 11234–11243. DOI: 10.1021/acsanm.3c03430.
37. Park, K. S., Ni, Z., Côté, A. P., Choi, J. Y., Huang, R., Uribe Romo, F. J., Chae, H. K., O'Keeffe, M., & Yaghi, O. M. (2006). Exceptional chemical and thermal stability of zeolitic imidazolate frameworks. Proceedings of the National Academy of Sciences, 103(27), 10186–10191. https://doi.org/10.1073/pnas.0602439103.
38. Tan, J. C., Fordham, S., Zuluaga, S., Cheetham, A. K., & Bennett, T. D. (2018). Mechanical resilience of zeolitic imidazolate framework ZIF 8: Pressure induced amorphization and recovery. Journal of the American Chemical Society, 140(25), 8551–8557. https://doi.org/10.1021/jacs.8b04744.
39. Becke, A. D. (1993). Density-functional thermochemistry. III. The role of exact exchange. Journal of Chemical Physics, 98(7), 5648–5652. https://doi.org/10.1063/1.464913
40. Lee, C., Yang, W., & Parr, R. G. (1988). Development of the Colle–Salvetti correlation-energy formula into a functional of the electron density. Physical Review B, 37(2), 785–789. https://doi.org/10.1103/PhysRevB.37.785
41. Frisch, M. J., Trucks, G. W., Schlegel, H. B., Scuseria, G. E., Robb, M. A., Cheeseman, J. R., … Fox, D. J. (2016). Gaussian 16, Revision C.01. Gaussian, Inc.
42. Wang, J., Wu, C., Dai, Y., Zhao, Z., Wang, A., Zhang, T., & Wang, Z. L. (2017). Achieving ultrahigh triboelectric charge density for efficient energy harvesting. Nature Communications, 8, 88. https://doi.org/10.1038/s41467-017-00131-4
43. Song, Giyoung; Kim, Younghoon; Yu, Seunggun; Min Ook Kim; Park, Sang Hee; Cho, Suk Man; Velusamy, Dhinesh Babu; Cho, Sung Hwan; Kim, Kang Lib; Kim, Jongbaeg; Kim, Eunkyoung; Park, Cheolmin. (2015).Molecularly Engineered Surface Triboelectric Nanogenerator by Self Assembled Monolayers (METS). Chemistry of Materials, 27(13), 4749–4755.https://doi.org/10.1021/acs.chemmater.5b01507.
44. Wang, Sihong; Zi, Yunlong; Zhou, Yusheng; Li, Shengming; Fan, Fengru; Lin, Long; Wang, Zhong Lin. (2016). Molecular surface functionalization to enhance the power output of triboelectric nanogenerators. Journal of Materials Chemistry A, 4(10), 3728–3734. https://doi.org/10.1039/C5TA10239A.
45. Brukerstein, J. I., Newbury, D. E., Joy, D. C., Lyman, C. E., Echlin, P., Lifshin, E., … Michael, J. R. (2003). Scanning Electron Microscopy and X-Ray Microanalysis (3rd ed.). Springer.
46. Guo, H., & Wang, Z. L. (2020). Triboelectric nanogenerators for self-powered sensors and systems. Advanced Materials, 32(48), 2002348. https://doi.org/10.1002/adma.202002348
47. García, R., & Pérez, R. (2002). Dynamic atomic force microscopy methods. Surface Science Reports, 47(6–8), 197–301. https://doi.org/10.1016/S0167-5729(02)00077-8
48. Beckelee Corporation. (2014). Dimension Icon Atomic Force Microscope User Manual (Version 8.15). Bruker Corporation.
49. Scherindelin, J., Arganda-Carreras, I., Frise, E., Kaynig, V., Longair, M., Pietzsch, T., … Cardona, A. (2012). Fiji: an open-source platform for biological-image analysis. Nature Methods, 9(7), 676–682. https://doi.org/10.1038/nmeth.2019
50. Rahman, M. T., Rana, S. M. S., Zahed, M. A., Lee, S., Yoon, E.-S., & Park, J. Y. (2022). MOF-derived nanoporous carbon incorporated nanofibers for high-performance triboelectric nanogenerators. Nano Energy, 94, 106921. https://doi.org/10.1016/j.nanoen.2022.106921
51. Roy, S., Lee, J. E., & Lee, C. (2019). Fabrication and performance evaluation of hybrid electromagnetic–triboelectric nanogenerators. Advanced Energy Materials, 9(30), 1901137. https://doi.org/10.1002/aenm.201901137
52. Velpula, M., Navaneeth, M., Potu, S., Mandal, T., & Bochu, L. (2024). High-performance MOF-303-based triboelectric nanogenerators for road energy harvesting. Journal of Materials Chemistry A, 12(10), 5000–5010. https://doi.org/10.1039/d4ta01247f

 doi:10.20944/preprints202507.1827.v1

53. Weigend, F., & Ahlrichs, R. (2005). Balanced basis sets of split valence, triple zeta valence and quadruple zeta valence quality for H to Rn: design and assessment of accuracy. Physical Chemistry Chemical Physics, 7(18), 3297–3305. https://doi.org/10.1039/b508541a
54. Huang, X., Wu, Q., Zhang, Q., Ding, W., & Wang, X. (2021). Enhancing low-frequency energy harvesting of triboelectric nanogenerators via surface microstructuring. Nano Energy, 80, 105512. https://doi.org/10.1016/j.nanoen.2021.105512
55. Cao, X., Pang, Y., Xu, L., Zhang, C., & Wang, Z. L. (2021). Integrated triboelectric nanogenerator array for simultaneous harvesting of water wave energy and wind energy. iScience, 24(5), 102440. https://doi.org/10.1016/j.isci.2021.102440
56. Gao, C., Zhao, J., Liu, T., Luo, B., Chi, M., … & Nie, S. (2024). Strong and stable woody triboelectric materials enabled by biphase blocking. Nano Letters, 24(24), 14932–14940. https://doi.org/10.1021/acs.nanolett.4c02802
57. Rigaku Oxford Diffraction. (2018). CrysAlisPro (Version 1.171.41.93a) [Data collection and processing software].
58. Dolomanov, O. V., Bourhis, L. J., Gildea, R. J., Howard, J. A. K., & Puschmann, H. (2009). OLEX2: a complete structure solution, refinement and analysis program. Journal of Applied Crystallography, 42(2), 339–341. https://doi.org/10.1107/S0021889808042726
59. Sheldrick, G. M. (2015b). Crystal structure refinement with SHELXL. Acta Crystallographica Section C, 71(Pt 1), 3–8. https://doi.org/10.1107/S2053229614024218
60. Sheldrick, G. M. (2015a). SHELXT – Integrated space-group and crystal-structure determination. Acta Crystallographica Section A, 71(Pt 1), 3–8. https://doi.org/10.1107/S2053273314026370
61. Keithley Instruments, Inc. (2018). Model 2450 SourceMeter® Source Measure Unit: User's Manual. Beaverton, OR: Keithley Instruments, Inc.
62. National Instruments. (2020). NI Measurement & Automation Explorer (MAX) User Manual (Document Number 378443A 01). Austin, TX: National Instruments.